ADVANCED MATERIALS
www.advmat.de

Hydrogen-Deficient Chain-Like Molecular Structure Confined Hydride Electrolyte for High-Voltage All-Solid-State Lithium Metal Batteries

Panyu Gao, Shunlong Ju, Tian Xu, Wubin Du, Yong Gao, Yaxiong Yang, Zhenglong Li, Hongyu Zhang, Yuqin Huang, Guanglin Xia, Fei Wang,* and Xuebin Yu**

The practical application of $LiBH_4$ in all-solid-state Li metal batteries (ASSLMBs) is hindered by low Li-ion conductivity at room temperature, poor oxidative stability, and severe dendrite growth. Herein, porous $[LiNBH]_n$ with a hydrogen-deficient chain-like molecular structure are designed for in situ space-confining $LiBH_4$, which enables strong attraction of negatively charged $H^{\delta-}$ atoms of $[BH_4]^-$ anions by Li^+ of $[LiNBH]_n$ chains that weakens Coulombic interaction between Li^+ and $[BH_4]^-$ anions and hence promotes Li ion diffusion. Additionally, the electron-withdrawing effect of $[LiNBH]_n$ chains induces the local electron localization of $LiBH_4$ that enhances oxidative stability of $LiBH_4$. Therefore, the Li ion conductivity of $LiBH_4$ reaches 2.2×10^{-4} S cm^{-1} at 30 °C, nearly 4 orders of magnitude higher than that of $LiBH_4$, with a voltage window of 5 V. Moreover, the interaction between Li metal and $[LiNBH]_n$ chains results in in situ formation of ultrathin layer composed of Li_3N and LiB alloys that hinders Li dendrites growth, leading to a critical current density value of 7.5 mA cm^{-2} and a cycling life of 100 h at 4 mA cm^{-2} with an overpotential of 125 mV. Hence, $LiCoO_2$|$LiBH_4$-70LiNBH|Li cell at 0.5 C deliver a high capacity of 89.5 mA h g^{-1} after 400 cycles.

1. Introduction

With the increasing demand for energy and the in-depth understanding of the importance of sustainable development of society and economy, Li-ion batteries (LIBs) characterized by high energy storage efficiency and environmental protection is under rapid development.[1] Replacing the applied graphite anode in current LIBs with Li metal anode has been widely regarded as a promising solution to increase the energy density of LIBs due to its high theoretical capacity (3860 mAh g^{-1}) and low electrochemical potential (−3.04 V versus standard hydrogen electrode, SHE).[2] Nonetheless, due to the highly reducible nature of Li metal anode, the serious side reactions with liquid organic electrolytes in the state-of-the-art LIBs, however, leads to low Coulombic efficiencies and inferior cycling stability and even safety issues caused by the continuous formation of Li dendrites and the flammable nature of organic electrolytes.[3] As a result, the development of all-solid-state Li-metal batteries (ASSLMBs) using nonflammable solid-state electrolytes (SSEs) with reliable thermal stability and high ionic conductivity have attracted wide intention.[4]

The search for solid-state electrolytes that have good interfacial capability with Li metal anode has made significant progress over the past few decades.[5] Unfortunately, most inorganic SSEs, including halide,[6] sulfide,[7] garnet,[8] and perovskite SSEs,[9] are highly reactive with Li metal anodes, leading to the continuous degradation of materials structures and thus electrochemical performance. In this regard, $LiBH_4$-based electrolytes that hold high thermodynamic stability against Li metal and high compressibility for high energy density attract particular interest.[10] Unfortunately, $LiBH_4$ electrolyte suffers from an ultralow Li-ion conductivity of 10^{-8} S cm^{-2} at room temperature, poor oxidative stability, and severe Li dendrite formation with a limited critical current density (CCD) of only 2.8 mA cm^{-2} at 125 °C.[11]

The main initial research focus is to enhance Li-ion conductivity of $LiBH_4$ via weakening the electrostatic interaction between Li^+ and $[BH_4]^-$ anions based on the chemical composition modification, including cation complexation and the synthesis of new compounds through the incorporation of a second species. Recent studies demonstrate that the introduction of oxides (e.g., Al_2O_3,[12] SiO_2,[13] etc.) could lead to the formation of a defect-rich interfacial layer that is able to improve the Li ion mobility through space charge layers. The limited electrochemical stability of $LiBH_4$, however, is induced by the severe oxidative decomposition of $[BH_4]^-$ anions, which exhibit poor thermodynamic stability of $[BH_4]^-$ anions owing to the easy delocalization of local electrons.[14] Hence, one of the effective strategies to enhance

P. Gao, S. Ju, T. Xu, H. Zhang, Y. Huang, G. Xia, F. Wang, X. Yu
College of Smart Materials and Future Energy
Fudan University
Shanghai 200433, China
E-mail: xiaguanglin@fudan.edu.cn; feiw@fudan.edu.cn; yuxuebin@fudan.edu.cn
W. Du, Y. Gao, Y. Yang, Z. Li
Institute of Science and Technology for New Energy
Xi'an Technological University
Xi'an 710021, China

The ORCID identification number(s) for the author(s) of this article can be found under https://doi.org/10.1002/adma.202508008

DOI: 10.1002/adma.202508008

oxidative stability of $LiBH_4$ SSEs is anion engineering, such as the introduction of stable halides and sulfides and the formation of polyhedral borates.[15] Unfortunately, induced by the high electronic conductivity at grain boundaries for SSEs, the severe growth of Li dendrites poses a major obstacle for the practical application of $LiBH_4$ SSEs.[16] Although this issue could be alleviated by reducing electronic conductivity of $LiBH_4$ SSEs via the introduction of electronically insulating fillers (e.g., MgO, LiF, etc.), its role in suppressing the growth of Li dendrites remains limited due to the ignorance of control over the interfacial contact between $LiBH_4$ SSEs and Li metal anode, which would lead to large interfacial resistance that promotes the continuous formation of Li dendrites and finally results in short circuits or micro short circuits within ASSLMBs.[17] Therefore, an effective strategy to simultaneously improve all the above-mentioned issues needs to be developed for the ultimate application of $LiBH_4$ SSEs.

Herein, we report in situ space-confinement of $LiBH_4$ into porous $[LiNBH]_n$ with a chain-like molecular structure (denoted as LiNBH) to simultaneously improve Li-ion conductivity and oxidative stability of $LiBH_4$ SSEs and especially suppress the formation of Li dendrites when using $LiBH_4$ as SSEs. This approach is realized by the formation of porous LiNBH induced by bubbling effect during the hydrogen desorption of $LiNH_2BH_3$ in the ball-milled composite of $LiBH_4$ and $LiNH_2BH_3$, followed by in situ confinement of melting $LiBH_4$. The hydrogen-deficient structure of porous LiNBH enables strong attraction of negatively charged $H^{\delta-}$ atoms of $[BH_4]^-$ anions by Li^+ of LiNBH induced by the enhanced electron-deficient B and N atoms of $[N_2BH]_n$ unit owing to the loss of hydrogen during the decomposition of $LiNH_2BH_3$. This leads to the deformation of $[BH_4]^-$ anions in $LiBH_4$ and hence the weakening of the Coulombic interaction between Li^+ and $[BH_4]^-$ anions, resulting in the decrease of the Li-ion diffusion barriers observed at the interface between porous LiNBH and $LiBH_4$ down to 0.069 eV that is 1.7 times lower than $LiBH_4$. Interestingly, the electron-withdrawing effect of LiNBH induces the local electron localization of $LiBH_4$ that blocks its electronic exchanges, which leads to the decreased electronic conductivity of $LiBH_4$ and the increased oxidative stability of $LiBH_4$. As a result, coupled with homogeneous interfaces between $LiBH_4$ and porous LiNBH enabled by in situ space-confinement strategy, the Li ion conductivity of $LiBH_4$ reaches 2.2×10^{-4} S cm^{-1} at 30 °C, which is nearly 4 orders of magnitude higher than that of $LiBH_4$, with a stable voltage window of 5 V. This wide oxidative stability helps minimize parasitic side reactions at high voltages, thereby preserving the integrity of the Li/SE interface. A stable interface, in turn, is essential for ensuring uniform lithium-ion flux and effectively suppressing the nucleation and growth of lithium dendrites. More importantly, the interaction between Li metal and LiNBH results in the in situ formation of ultrathin layer composed of Li_3N with high Li-ion conductivity and LiB alloys with high lithiophilic property with a high average Young's modulus of 27.96 GPa, which not only contributes to the building of uniform interfaces between the electrolyte and Li metal anode, but also guides the homogenous Li plating and blocks the growth of Li dendrites. This synergistically enhances the capability of $LiBH_4$-70LiNBH in alleviating the growth of Li dendrites, leading to a critical current density (CCD) value of 7.5 mA cm^{-2} and a stable cycling life of 100 h at a high current density of 4 mA cm^{-2} with an overpotential of only 125 mV. As a result, the ASSLMBs of $LiCoO_2$/$LiBH_4$-70LiNBH/Li cell impressively deliver a high capacity of 89.5 mA h g^{-1} at 0.5 C after 400 cycles with a capacity retention of 85.4%.

2. Results and Discussion

As schematically illustrated in **Figure 1a**, $LiBH_4$-$x$$LiNH_2BH_3$ composites with a weight ratio of x%, $LiBH_4$-$x$$LiNH_2BH_3$ composites with a weight ratio of x% for $LiNH_2BH_3$ obtained by facile mechanical milling $LiBH_4$ and $LiNH_2BH_3$ are heated at 200 °C for hydrogen desorption process, during which $LiNH_2BH_3$ would inflate and become loose and porous induced by violent hydrogen desorption (Figure S1, Supporting Information). After complete dehydrogenation, $LiNH_2BH_3$ is in situ transformed to porous $[LiNBH]_n$ scaffolds (denoted as LiNBH) based on the combination of N-H and B-H bonds.[18] Finally, the mixture is heated at 300 °C under a hydrogen pressure of 100 atm for the complete melting of $LiBH_4$ into as-formed porous LiNBH scaffolds, during which $LiBH_4$-$x$$LiNH_2BH_3$ composites would be transformed into solid-state $LiBH_4$-xLiNBH electrolytes. To characterize the confinement structure, pore size distribution analysis of the LiNBH framework (Figure S1f, Supporting Information) reveals that the pores range from 0.1 to 0.6 μm, with an average diameter of ≈0.266 μm.

X-ray diffraction (XRD) patterns of $LiBH_4$-$x$$LiNH_2BH_3$ composites with various mass ratios demonstrate the presence of $LiNH_2BH_3$ and $LiBH_4$ (Figure 1b and Figure S2, Supporting Information). After mechanical milling with $LiNH_2BH_3$, the crystallinity of $LiBH_4$ declines and only weak diffraction peaks of $LiBH_4$ could be observed. When the stoichiometric ratio of $LiNH_2BH_3$ to $LiBH_4$ increased, no new phase is detected, which coincides well with the fourier transform infrared (FTIR) results (Figure S3, Supporting Information). Upon heating to 300 °C, obvious hydrogen release could be observed for $LiNH_2BH_3$ with a weight loss of 10.8 wt.% (Figure S4, Supporting Information) attributed to the intramolecular polymerization of $LiNH_2BH_3$ via the combination of B-H and N-H bonds toward the formation of amorphous LiNBH,[19] which could be verified by the weakening of B-H and N-H bonds in FTIR spectra. After the high-temperature dehydrogenation reaction, XRD pattern of the resulting $LiBH_4$−xLiNBH composite shows the complete disappearance of the characteristic peaks of $LiNH_2BH_3$, while only the characteristic peaks of $LiBH_4$ remain unchanged (Figure 1d). This demonstrates that $LiNH_2BH_3$ is completely transformed into amorphous LiNBH during the reaction, as further proved by high-resolution transmission electron microscope (HRTEM) image (Figure S5, Supporting Information). It is noted that after spatial confinement, the diffraction peak at $2\theta \approx 22°$ is significantly enhanced in the XRD pattern. This enhancement mainly results from the structural evolution of $LiBH_4$ during ball milling and thermal annealing (Figure S6, Supporting Information). Thermal annealing process may facilitate recrystallization and preferential growth along thermodynamically stable planes. Meanwhile, ball milling process may break the original texture, lead to randomized orientations, and increase the exposure of previously underrepresented planes, thereby enhancing the intensity of the corresponding diffraction peak. Fortunately, the peaks of $LiBH_4$ in FTIR spectra remained almost unchanged, indicating the formation of amorphous $LiBH_4$. Furthermore, differential scanning

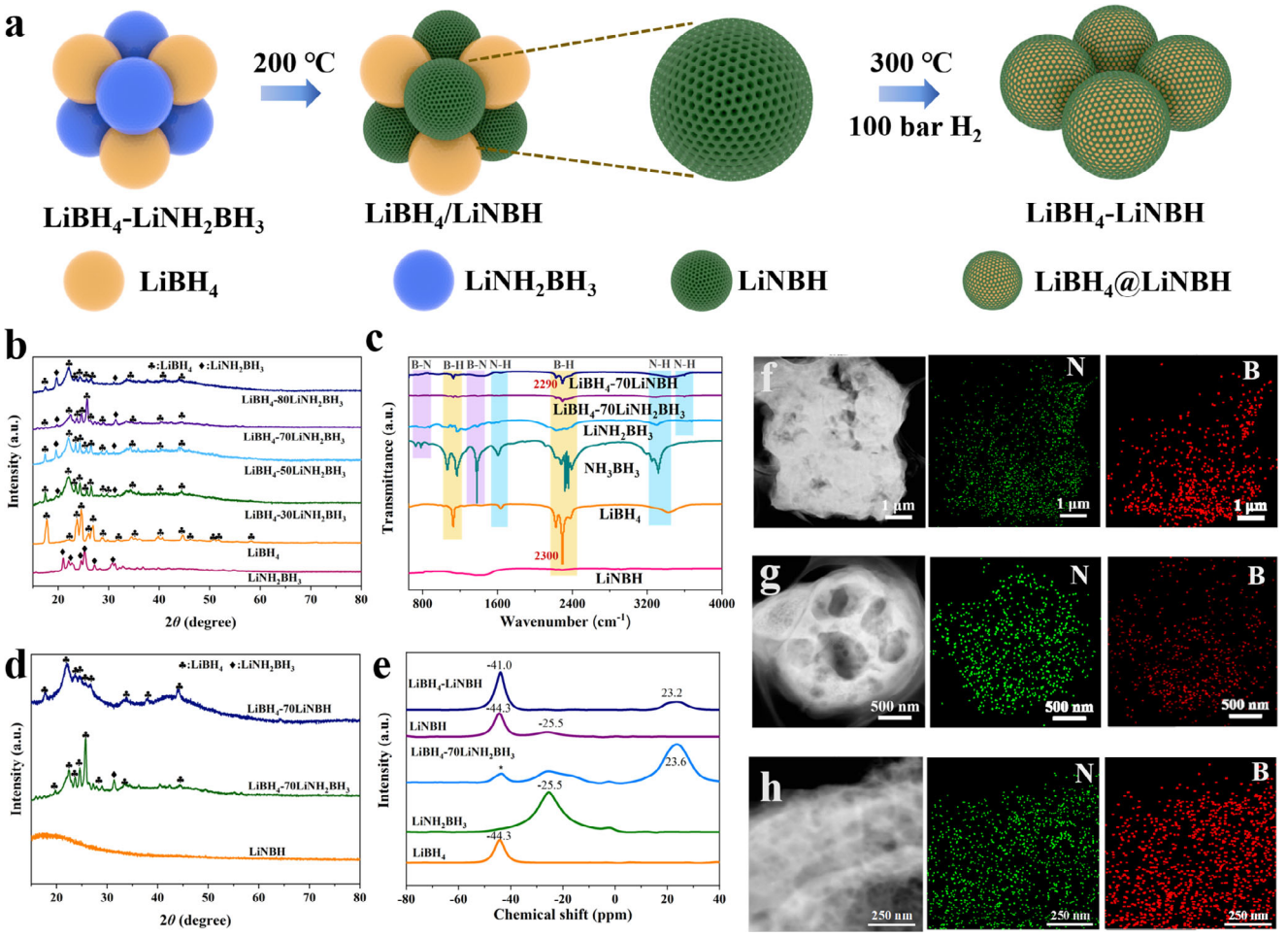

Figure 1. a) Schematic diagram of the preparing process of solid-state $LiBH_4$-*x*LiNBH electrolytes. b) XRD patterns and c) FTIR spectra of the as-synthesized $LiBH_4$-*x*$LiNH_2BH_3$ and thus-obtained $LiBH_4$-*x*LiNBH electrolytes, with $LiBH_4$ and $LiNH_2BH_3$ included for comparison. d) XRD patterns and e) solid-state ^{11}B NMR spectra of $LiBH_4$-70LiNBH, with $LiNH_2BH_3$ and $LiBH_4$-70$LiNH_2BH_3$ included for comparison. TEM images of f) $LiNH_2BH_3$, g) LiNBH, and h) $LiBH_4$-70LiNBH and their corresponding EDS elemental mapping images.

calorimetry (DSC) results demonstrate that a characteristic phase transformation temperature of pure $LiBH_4$ could be observed at 110 °C with a melting temperature of 287 °C while no endothermic peak could be observed for LiNBH, indicating the robust structure of the as-synthesized LiNBH (Figure S7, Supporting Information). As a result, a weak endothermic peak at 292 °C, corresponding to the melting of $LiBH_4$, could be detected in $LiBH_4$-70LiNBH electrolyte.

Transmission electron microscope (TEM) and scanning electron microscope (SEM) images demonstrate the microscopic morphology of $LiNH_2BH_3$ consisting of solid irregular particles (Figure 1f and Figure S1, Supporting Information). Besides, the SEM images of pure $LiBH_4$ reveal an irregular blocky structure with particle sizes ranging in the micron range (Figure S8, Supporting Information). Interestingly, uniform mesopores with irregular macropores could be observed for the as-synthesized LiNBH induced by the bubbling effect of hydrogen release during the decomposition of $LiNH_2BH_3$, which provides sufficient space for the melt infiltration of $LiBH_4$ (Figure 1g and Figure S1, Supporting Information). Therefore, after the heating process under the high-pressure hydrogen atmosphere for the melt infiltration of $LiBH_4$, large macropores are uniformly occupied by $LiBH_4$ in the as-synthesized $LiBH_4$-70LiNBH electrolyte (Figure 1h). The corresponding element mapping results validate the homogeneous distribution of B and N, which provides indirect evidence to in situ uniform space-confinement of $LiBH_4$ into porous LiNBH.

Solid-state ^{11}B nuclear magnetic resonance (NMR) is conducted to disclose the chemical environment of $LiBH_4$ during the formation of $LiBH_4$-*x*LiNBH electrolytes (Figure 1e). The characteristic BH_3 unit of $LiNH_2BH_3$ and BH_4 unit of $LiBH_4$ could be clearly detected at −25.5 and −44.3 ppm, respectively. After the hydrogen desorption from pure $LiNH_2BH_3$, the characteristic peak of BH_3 unit is almost disappeared with the detection of a new peak located at 23.6 ppm that could be indexed to $[N_2BH]_n$ unit with a chain-like molecular structure attributed to the intramolecular combination of B-H and N-H bonds, while the weak peak indexed at −25.3 ppm results from the slight presence of N-BH_3 unit at the terminal of the polymer-like LiNBH.[20] In addition, a comparative analysis was conducted on the total

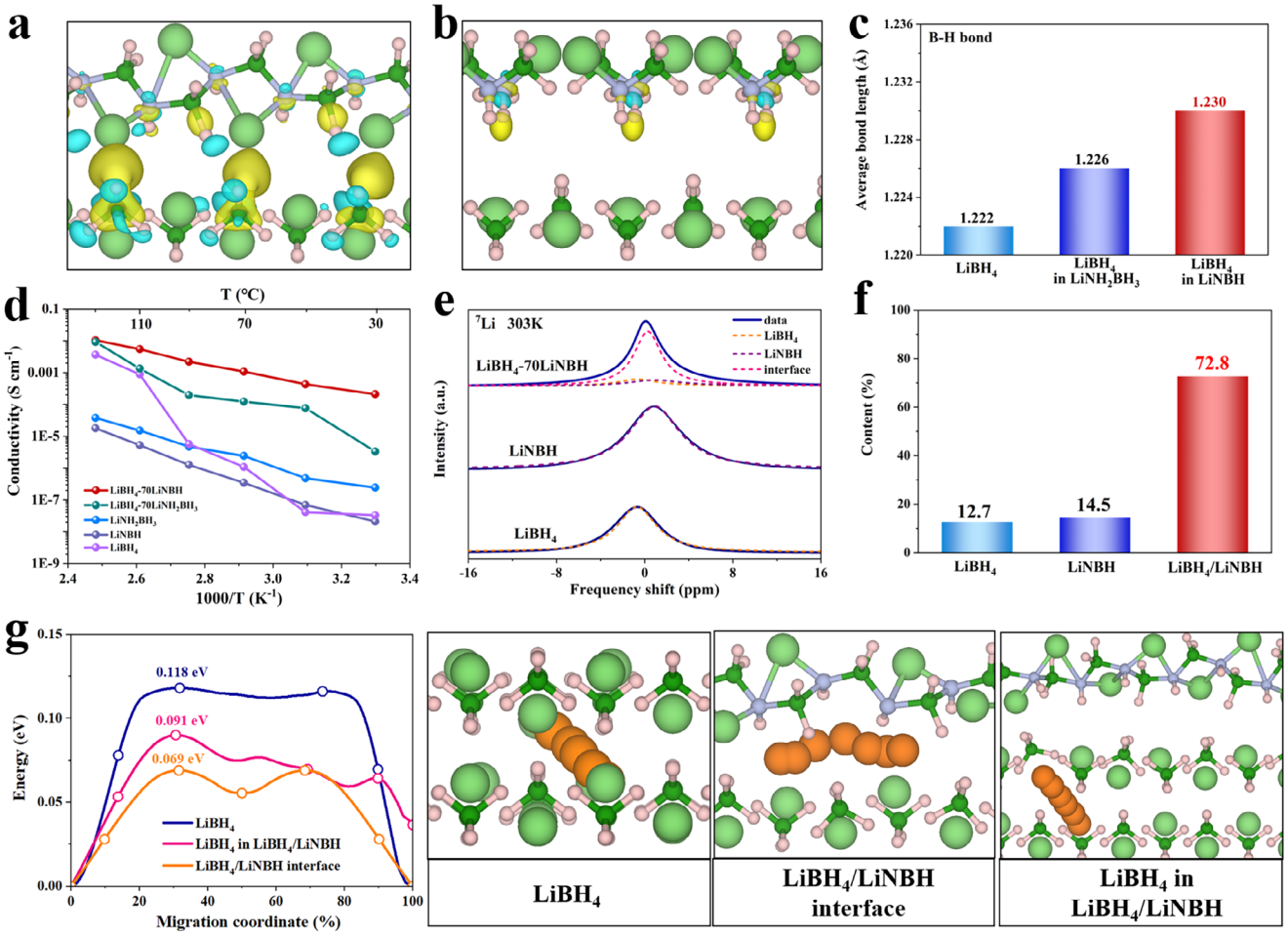

Figure 2. The charge density difference plot of the interface a) between LiNBH and $LiBH_4$ and b) between $LiNH_2BH_3$ and $LiBH_4$. The light green, dark green, purple, and pink balls present Li, B, N, and H atoms, respectively. The yellow area represents the gathering of electron and the blue area represents the deficiency of electron. c) The average B-H bond length of $LiBH_4$ and $LiBH_4$ in $LiBH_4/LiNH_2BH_3$ composite and $LiBH_4$/LiNBH composite, respectively. d) Arrhenius ionic conductivity plots of $LiBH_4$, LiNBH, $LiNH_2BH_3$, $LiBH_4$-70$LiNH_2BH_3$ and $LiBH_4$-70LiNBH. e) Solid-state ^{7}Li NMR spectra of $LiBH_4$, LiNBH and $LiBH_4$-70LiNBH. f) The calculated contents of the broad NMR peak belonging to $LiBH_4$ and LiNBH, and the narrow NMR peak belonging to the interface between $LiBH_4$ and LiNBH. g) The energy profile of Li-ion diffusion pathways in $LiBH_4$, $LiBH_4$ in LiNBH/$LiBH_4$ composite and the interface between LiNBH and $LiBH_4$ along the corresponding Li-ion diffusion pathways.

energy of bulk LiNBH and chain-like $[LiNBH]_n$ molecular structures (Figure S9, Supporting Information). The total energy of the chain-like $[LiNBH]_n$ molecular structure is −192.04 eV, which is significantly lower than that of bulk LiNBH (−190.50 eV), indicating that the chain-like $[LiNBH]_n$ molecular structure is thermodynamically more stable, which coincides well with the previously reported results.[21] Moreover, we observed the characteristic peak of $[BH_4]^-$ at −43.5 ppm in LiNBH, which is likely due to minor side reactions during the dehydrogenation process of $LiNH_2BH_3$.[22] The characteristic BH_3 unit of $LiNH_2BH_3$ at −25.5 ppm and BH_4 unit of $LiBH_4$ at −44.3 ppm, which are identical to that in pure $LiNH_2BH_3$ and $LiBH_4$, could be clearly observed in the as-synthesized $LiBH_4$-$x$$LiNH_2BH_3$ composites. Interestingly, after identical heating process for hydrogen desorption from the as-synthesized $LiBH_4$-$x$$LiNH_2BH_3$, although the typical peaks of BH_4 unit of $LiBH_4$ and $[N_2BH]_n$ unit of $[LiNBH]_n$ could still be detected, a clear downfield shift by ≈3.3 ppm is observed for BH_4 unit of $LiBH_4$-70LiNBH in comparison to pure $LiBH_4$, which could be attributed to strong attraction of negatively charged $H^{\delta-}$ atoms of $[BH_4]^-$ anions by Li^+ of LiNBH induced by the enhanced electron-deficient B and N atoms of $[N_2BH]_n$ unit owing to the loss of hydrogen during the decomposition of $LiNH_2BH_3$ as evidenced by the obvious charge transfer of 0.038|e| between $[BH_4]^-$ anions and LiNBH (**Figure 2a**). The upfield shift of $[N_2BH]_n$ unit by 0.4 ppm provides direct evidence to the interaction strong affinity between LiNBH and $LiBH_4$. In addition, only the characteristic peaks of the BH_4 unit and the $[N_2BH]_n$ structure are observed in the $LiBH_4$–LiNBH composite, indicating that the $[LiNBH]_n$ chains remains stable at elevated temperatures without structural transformation. Therefore, H atoms would be pulled away from the B atoms of $[BH_4]^-$ anions and the average length of B-H bonds $LiBH_4$ under the presence of LiNBH is increased to 1.23 Å (Figure 2c), 0.65% longer than that of pure $LiBH_4$, leading to the deformation of $[BH_4]^-$ anions in $LiBH_4$ and hence the weakening of the Coulombic interaction between Li^+ and $[BH_4]^-$ anions, which would promote the

Li diffusion kinetics of $LiBH_4$. By comparison, only weak interaction could be observed between $[BH_4]^-$ anions in $LiBH_4$ and $LiNH_2BH_3$ with a charge transfer of 0.005|e| (Figure 2b), which is 7.6 times lower than that between $[BH_4]^-$ anions and LiNBH and hence the B-H bond length remains almost unchanged for $LiBH_4$ under the presence of $LiNH_2BH_3$. These results demonstrate the important role of hydrogen desorption of $LiNH_2BH_3$ in reinforcing charge transfer between $LiBH_4$ electrolyte and LiNBH and hence weakening the Coulombic interaction between Li^+ and $[BH_4]^-$ anions, which is capable of enhancing Li ion conductivity of $LiBH_4$.

The symmetric cells consisting of SUS|SSE|SUS (SUS: stainless steel) with various electrolytes are first assembled to assess their real Li-ion conductivities using electrochemical impedance spectroscopy (EIS) method. According to the Arrhenius plots of EIS results, the temperature-dependent conductivities of various $LiBH_4$-*x*LiNBH electrolytes are calculated (Figure 2d and Figure S10, Supporting Information). In the term of pure $LiBH_4$, its Li ion conductivity is only 3.23×10^{-8} S cm^{-1} at 30 °C and the characteristic abrupt increase in Li ion conductivity to 8.83×10^{-4} S cm^{-1} at a temperature as high as 110 °C, corresponding to the phase transformation from *Pnma* phase to $P6_3mc$ phase, could be clearly observed. By comparison, the logarithmic conductivity of various $LiBH_4$-*x*LiNBH electrolytes is linearly decreased with reciprocal temperature ($1/T$) with the absence of the abrupt reduction in conductivity at 110 °C. It is worth noting that the ionic conductivity of the $LiBH_4$-*x*LiNBH electrolyte first increases and then decreases with the increase in LiNBH content. It is due to that LiNBH itself does not exhibit high ionic conductivity. The ionic conductivity of LiNBH at room temperature is determined to be only 2.1×10^{-8} S cm^{-1}, which is even lower than that of $LiBH_4$. Therefore, when the content of LiNBH becomes excessive, although the number of interfaces increases, the reduced content of the conductive phase $LiBH_4$ limits the overall ionic conductivity of the composite electrolyte. As a result, the as-synthesized $LiBH_4$-70LiNBH electrolyte delivers the highest ion conductivity over the range of temperature and it reaches 2.2×10^{-4} S cm^{-1} at 30 °C (Figure S11, Supporting Information), which is nearly 4 orders of magnitude higher than that of $LiBH_4$. Meanwhile, it is noted that the ion conductivity of LiNBH is determined to 2.1×10^{-8} S cm^{-1} only at room temperature, even lower than that of $LiBH_4$, indicating the important role of the interfaces between LiNBH and $LiBH_4$ in improving Li ion conductivity of $LiBH_4$. Interestingly, only an ultralow of Li-ion conductivity of 3.3×10^{-6} S cm^{-1} at room temperature could be achieved for $LiBH_4$-70$LiNH_2BH_3$ electrolyte, which provides direct evidence to the important role of electron-deficient LiNBH with a chain-like molecular structure induced by the hydrogen desorption of $LiNH_2BH_3$ in improving Li ion conductivity of $LiBH_4$. Additionally, after heating, NH_3BH_3 also expands to form a porous structure, which could undergo a similar confinement reaction with $LiBH_4$. To further verify the advanced confinement effect of using LiNBH, a composite of $LiBH_4$ and NH_3BH_3 in the same ratio is prepared and heated using the same method of $LiBH_4$-70LiNBH, resulting in the formation of $LiBH_4$ confined into porous product of the dehydrogenated NH_3BH_3 (denoted as $LiBH_4$-70NHBH). As shown in Figure S12, Supporting Information, the Li ion conductivity of $LiBH_4$-70NHBH at room temperature is 2×10^{-6} S cm^{-1}. Although this value is higher than that of pure $LiBH_4$, the increase in Li-ion conductivity throughout the entire tested temperature range is significantly less pronounced than that observed in the $LiBH_4$-70LiNBH system. This result further highlights the significant effect of the confinement role LiNBH in improving ionic conductivity of $LiBH_4$. The activation energy of $LiBH_4$-70LiNBH electrolyte according to Arrhenius plots is calculated to be 0.44 eV (Figure S13, Supporting Information), even much lower than high-temperature $P6_3mc$ phase of $LiBH_4$ (i.e., 0.905 eV), which is also a typical activation energy for super ionic conductors (<0.5 eV).[23] Moreover, AIMD simulations on $LiBH_4$, LiNBH and $LiBH_4$/LiNBH at 30 °C are performed. As shown in Figure S14, Supporting Information, after the combination of $LiBH_4$ and LiNBH, the mean-square displacements (MSD) value of Li^+ in the composite material significantly increases, indicating a larger displacement over the same time period, demonstrating greater migration freedom and activity. Furthermore, the lithium diffusion coefficients are calculated from the MSD using the Einstein relation.[24] The calculations show that the total self-diffusion coefficients of $LiBH_4$, LiNBH, and the $LiBH_4$-LiNBH composite at 30 °C are 5.6×10^{-10}, 2.96×10^{-9}, and 4.17×10^{-9} cm^2 s^{-1}, respectively. These results indicate that the diffusion rate of lithium ions in the $LiBH_4$-LiNBH composite is significantly higher than that in pure $LiBH_4$ and LiNBH, further confirming the synergistic effect generated during the composite process. This finding suggests that the confined structure of LiNBH provides an effective pathway for the rapid migration of Li ions. More importantly, according to the direct current polarization results, the Li-ion transference number of $LiBH_4$-70LiNBH is calculated to be 0.9998 at 30 °C and 0.9991 at 60 °C (Figure S15, Supporting Information), respectively, and, owing to the ultralow electronic conductivity of LiNBH (7.3×10^{-10} S cm^{-2}), the electronic conductivity of the resulting $LiBH_4$-70LiNBH is measured to be 2.7×10^{-8} S cm^{-2} at room temperature, which is 9.8 folds lower than that of $LiBH_4$ (Figure S16, Supporting Information). The electronic conductivity of $LiBH_4$-70LiNBH reaches 32.7 folds lower than that of $LiBH_4$ upon heating to 60 °C. These results demonstrate that $LiBH_4$-70LiNBH is a single Li-ion conductor and LiNBH that are uniformly distributed play an electronic blocking role inside of the as-synthesized $LiBH_4$-70LiNBH electrolyte.

Subsequently, solid-state ^7Li nuclear magnetic resonance (NMR) spectroscopy is conducted at room temperature to analyze the coordination environment shift of Li^+ in the $LiBH_4$-70LiNBH (Figure 2e). The transverse relaxation time (*T2*) is closely related to the ion conductivity, which is inversely proportional to the full width at half maximum (FWHM) of the NMR peaks. After space-confinement of $LiBH_4$ into LiNBH, the FWHM of NMR peak became smaller (Figure S17, Supporting Information) that would be divided into two individual Gaussian peaks, in which the broad one reflects Li ion migration in bulk $LiBH_4$ and LiBNH and the sharp one reflects the faster mobility averaging the dipolar and quadrupolar interactions, corresponding to the presence of high-mobility Li ions that occurs at the interface between $LiBH_4$ and LiBNH.[25] The content of the component with high Li ion mobility in $LiBH_4$-70LiNBH is calculated to be 72.8% (Figure 2f), which further confirms the advantage of the lithium-ion conductivity in the composite electrolyte. In addition, we performed temperature-dependent ^7Li solid-state NMR measurements on the $LiBH_4$-LiNBH composite electrolyte. As shown in Figure S18,

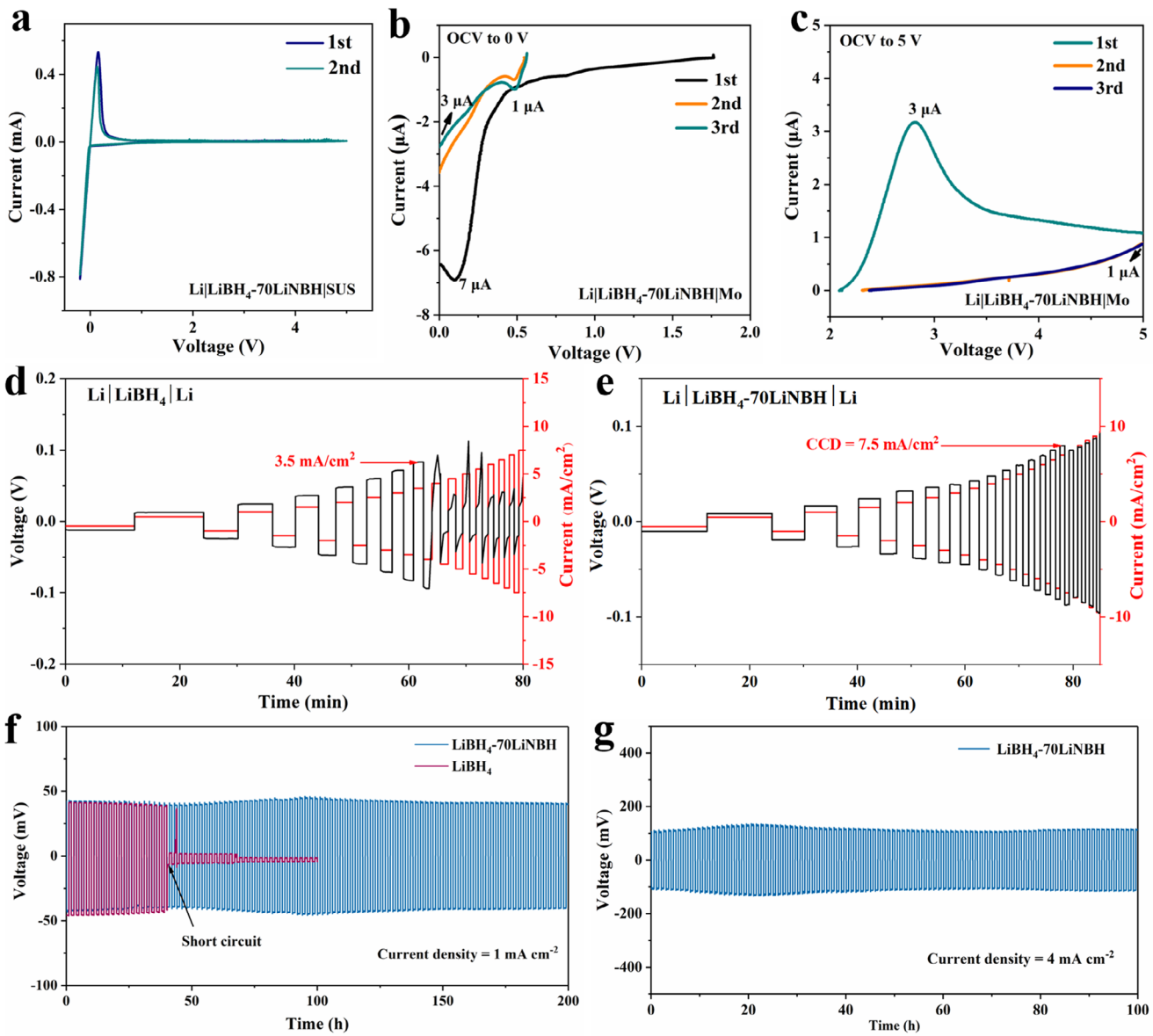

Figure 3. CV curves of $LiBH_4$-70LiNBH within the potential windows of a) -0.2 to 5 V OCV to b) 0 V, and OCV to c) 5 V at a scan rate of 0.025 mV s^{-1}. Voltage profiles of the bare Li symmetric cell using d) $LiBH_4$ and e) $LiBH_4$-70LiNBH electrolyte during galvanostatic discharging/charging tests at step-increased current densities. The galvanostatic cycling curves of the $LiBH_4$-70LiNBH based symmetrical Li cell at the current density of g) 1 mA cm^{-2} and f) 4 mA cm^{-2}. All measurements were conducted at 60 °C, except for the Li|$LiBH_4$|Li symmetric cell tested at 120 °C.

Supporting Information, the FWHM of the ^7Li peak gradually decreases with increasing temperature, which is consistent with the trend of enhanced Li-ion conductivity at elevated temperatures. This observation demonstrates that LiNBH confinement effectively enhances Li-ion mobility in the composite. Moreover, the ^1H NMR spectroscopy at room temperature on $LiBH_4$-70LiNBH, $LiBH_4$-70$LiNH_2BH_3$, and $LiBH_4$ is shown in Figure S19, Supporting Information. It can be noted that the FWHM of $LiBH_4$-70$LiNH_2BH_3$ and $LiBH_4$ are 4.22 and 3.43 ppm, respectively. After the confinement reaction, the ^1H characteristic peak of $LiBH_4$-70LiNBH becomes narrower with an FWHM of 3.12 ppm, which is significantly smaller than those of the other two samples. This indicates that in $LiBH_4$-70LiNBH, the motion of the $[BH_4]^-$ group is enhanced, leading to a shortened relaxation time and a narrower peak shape, which in turn facilitates Li ion migration, indicating the formation of uniform interfaces between $LiBH_4$ and LiNBH, which provides indirect evidence to the homogeneous distribution of $LiBH_4$ inside of LiNBH owing to the uniform confinement of $LiBH_4$ into porous LiBNH.

To further understand the mechanism behind the improvement of ion conductivity in $LiBH_4$-70LiNBH electrolyte, the energy barriers of Li diffusion are investigated density functional theory (DFT) calculations. It is revealed that the diffusion barrier of Li ions approaches 0.118 eV for $LiBH_4$ (**Figure 3g**) and 0.178 eV for LiNBH (Figure S20, Supporting Information). In strong contrast, after incorporation of $LiBH_4$ into LiNBH, the

Li-ion diffusion barriers of $LiBH_4$ and LiNBH in $LiBH_4$-70LiNBH electrolyte are decreased to 0.091 and 0.141 eV, respectively. It could be attributed to the increase of Li-N bonds of LiNBH and Li-H bonds of $LiBH_4$ in $LiBH_4$-70LiNBH to 2.28 and 2.24 Å (Figure S21, Supporting Information), respectively, in comparison with bulk LiNBH (2.08 Å) and $LiBH_4$ (2.16 Å) owing to the strong affinity between B and N atoms of $[N_2BH]_n$ unit and $LiBH_4$. This structural change is also supported by the FTIR results in Figure 3c, where the characteristic B–H stretching vibration peak shifts from 2300 cm^{-1} in pure $LiBH_4$ to 2290 cm^{-1} in the $LiBH_4$-70LiNBH composite, indicating that the B-H bonds in $LiBH_4$ are elongated under the influence of LiNBH, leading to weakened bond strength. Consistent with these observations, we also note that in earlier structural characterizations, the (101) lattice spacing of $LiBH_4$ reaches 0.508 nm (FiguresS5b,c, Supporting Information), clearly larger than the reference value of 0.494 nm for the P*nma* phase in the PDF database. Similarly, the (011) lattice spacing increases from 0.371 to 0.375 nm. These results confirm that the elongation of B–H bonds leads to an increase in the volume of the BH_4^- tetrahedral units, which propagates through the crystal structure, resulting in overall lattice expansion. To further investigate the structural influence of LiNBH on $LiBH_4$, electron energy loss spectroscopy (EELS) measurements were performed on both $LiBH_4$ and $LiBH_4$-70LiNBH. As shown in Figure S22, Supporting Information, the main π^* transition peak in the B K-edge spectrum of $LiBH_4$, originally located at 188.6 eV and shifts clearly to a lower energy position at 187.9 eV after confinement of LiNBH, indicating that the B-H bond is elongated and its covalent character is weakened, leading to a reduced energy loss associated with the B 1s to π^* transition. More interestingly, the lowest Li ion diffusion barrier of 0.069 eV that is 1.7 times lower than $LiBH_4$ is observed at the interface between LiNBH and $LiBH_4$. By comparison, the presence of $LiNH_2BH_3$ exhibits limited effect in increasing Li-H bond of $LiBH_4$ (Figure S23, Supporting Information). These results demonstrate that the space-confinement effect of LiNBH weakens the coulombic interaction between Li^+ and $[BH_4]^-$ anions and promotes the formation of continuous interfaces between $LiBH_4$ and LiNBH. Under the confinement role of LiNBH, the $LiBH_4$ lattice undergoes local distortion induced by stress, generating more low-energy interstitial sites that facilitate Li^+ deintercalation and migration. Additionally, a low-barrier interfacial layer forms at the $LiBH_4$-LiNBH contact region, serving as a preferential pathway for Li^+ migration. As a result, the Li^+ migration pattern shifts from 1D hopping within bulk $LiBH_4$ to interface-dominated multidimensional diffusion, fundamentally optimizing the migration mechanism and explaining the significantly enhanced conductivity observed in the confined structure. Unlike pure $LiBH_4$, where Li^+ ions migrate solely within the bulk phase, interface migration becomes the dominant pathway in the composite, leading to higher transport efficiency.

In order to unravel the mechanism behind this phenomenon, the total density of states (TDOS) and partial density of state (PDOS) of $LiBH_4$-70LiNBH is subsequently investigated, with $LiBH_4$ and $LiBH_4$-70$LiNH_2BH_3$ included for comparison (Figure S24, Supporting Information). The typical sp^3 hybridization of $[BH_4]^-$ of $LiBH_4$ and $[BH_3]$ group of $LiNH_2BH_3$ and sp^2 hybridization of $[NH_2]$ group of $LiNH_2BH_3$ could be found (Figure S25, Supporting Information). The bands of all atoms show only a slight increase for $LiBH_4$-70$LiNH_2BH_3$ owing to their weak interaction (Figure 2b). It is worth noting that after the combination of LiNBH and $LiBH_4$, the DOS as a whole shift toward lower energy levels. This attributed to the change of the Fermi level after the combination of the two materials, which leads to an overall shift of the DOS to the lower energy direction. Moreover, this combination effect indicates that the electronic structure has been significantly modified, suggesting a possible interaction between the two phases. Interestingly, the hydrogen desorption of $LiNH_2BH_3$ that owns a molecular dipole-moment of 4.68 Debye results in a higher dipole-moment of 5.48 Debye for LiNBH (Figure S26, Supporting Information), which leads to the increased electron-withdrawing effect and hence promotes the interaction between $LiBH_4$ and LiNBH. Therefore, the DOS of H, B, N, and Li of $LiBH_4$-70LiNBH are all changed in comparison with pure $LiBH_4$ and LiNBH with the observation of new peaks between −1.2 and −0.6 eV (Figure S24a, Supporting Information), indicating the local electron localization at this site attributed to the strong attraction of $LiBH_4$ by the hydrogen-deficient LiNBH (Figure 2a), which would impede the electron diffusion inside of $LiBH_4$-70LiNBH and hence result in the decreased electronic conductivity of $LiBH_4$-70LiNBH in comparison with pure $LiBH_4$ (Figure S16, Supporting Information). Furthermore, due to the strong interaction between LiNBH and $LiBH_4$, the Coulombic interaction between Li^+ and $[BH_4]^-$ anions is weakened, as evidenced by the obvious increase of Li-H bonds of $LiBH_4$ after the introduction of LiNBH (Figure S24b, Supporting Information), which directly contributes to promoting Li ion conductivity of $LiBH_4$-70LiNBH.

The electrochemical stability of $LiBH_4$-70LiNBH electrolyte is investigated using cyclic voltammetry (CV) of Li|$LiBH_4$-70LiNBH|SUS cell at a scanning rate of 0.025 mV s^{-1} (Figure 3a). In the potential windows of −0.2 to 5 V, only obvious redox peaks near 0 V that correspond to the Li plating and stripping on the SUS electrode could be observed. The overlap of peaks in terms of sharpness, intensity, and potential position during the subsequent cycles indicates the excellent electrochemical stability of $LiBH_4$-70LiNBH electrolyte. To avoid the interference of Li plating/stripping process, open-circuit voltage (OCV) tests of Li|$LiBH_4$-70LiNBH|Mo cells are further conducted to evaluate the electrochemical stability of $LiBH_4$-70LiNBH electrolyte. Upon scanning repeatedly from OCV to 0 V (Figure 3b) and 5 V (Figure 3c), only weak signals at 0.1 V (7 μA) and 2.8 V (3.0 μA) could be observed in the first cycle and these signals completely vanished in the following scans, indicating the stable formation of solid electrolyte interphase (SEI) and cathode electrolyte interphase (CEI) films. By comparison, in addition to the characteristic peaks of Li plating and stripping process, there are clear cathodic peaks at 1.0 and 2.2 V and anodic peaks at 0.5 V are detected for the Li|$LiBH_4$|Mo cell (Figure S27a, Supporting Information), indicating the serious decomposition of $LiBH_4$ at high potentials. It corresponds well with the result of OCV measurements of Li|$LiBH_4$|Mo cells, that exhibit numerous irregular peaks (Figure S27b,c, Supporting Information). These results directly demonstrate that the in situ formed SEI and CEI films enhances the electrochemical stability of $LiBH_4$ inside of $LiBH_4$-70LiNBH electrolyte.

The dendrite suppression capacity and the capability of $LiBH_4$-70LiNBH electrolyte is evaluated by galvanostatic cycling at increased current densities from 0.5 to 10 mA cm^{-2}. As the current

density increases step by step, the voltage correspondingly increases and only a critical current density (CCD) value of 3.5 mA cm^{-2} is observed for pristine $LiBH_4$ electrolyte (Figure 3d). By comparison, owing to the electron localization effect of B and N atoms of LiNBH that impedes the electron transfer of $LiBH_4$, the CCD value of $LiBH_4$-70LiNBH electrolyte is increased to 7.5 mA cm^{-2} (Figure 3e), which is 2.15 times higher than that of $LiBH_4$. Notably, as shown in Figure S28, Supporting Information, even at 30 °C, the $LiBH_4$-70LiNBH electrolyte still exhibits a high CCD of 6.5 mA cm^{-2} with only slight evidence of micro short-circuiting. This result further confirms its excellent interfacial stability and robust lithium-ion transport capability at room temperature. Moreover, long-term cycling Li plating and stripping performance is subsequently investigated at 1 mA cm^{-2} for the cell using $LiBH_4$-70LiNBH electrolyte, which delivers a voltage difference of 40 mV for 200 h, while the cell using $LiBH_4$ as the electrolyte fails after only 40 h of cycling (Figure 3f). More impressively, upon increasing the current density to 4 mA cm^{-2}, equaling to over 0.5 times the CCD value, the cell using $LiBH_4$-70LiNBH electrolyte still delivers stable cycling performance without obvious voltage differences fluctuations, exhibiting an overpotential of only 125 mV after 100 h (Figure 3g), which provides further evidence to the cycling stability of $LiBH_4$-70LiNBH electrolyte in suppressing the formation of Li dendrites. The corresponding ultralow overpotential is also significantly superior to most recently reported solid-state electrolytes (Table S1, Supporting Information) and even comparable to that of liquid-state electrolytes.

To gain insight into the enhanced capability of $LiBH_4$-70LiNBH electrolyte in suppressing the formation of Li dendrites, the chemical environment of Li metal upon cycling is further investigated by X-ray photoelectron Spectroscopy (XPS) after cycling. The cycled Li|SE|Li cell was disassembled in an argon-filled glovebox, and the lithium metal was rinsed with THF to dissolve residual $LiBH_4$. A clean, flat interface area was then selected for XPS analysis. Except the possible the formation of Li_2O during the sample transfer process, only the characteristic peak of Li metal is observed for Li metal anode before and after cycling in Li 1s XPS spectra (**Figure 4a**) without the detection of any B-containing or N-containing species in B 1s XPS spectra owing to the thermodynamic stability of $LiBH_4$ against Li metal (Figure 4b,c). Interestingly, the distinct peaks assigned to Li_3N, as well as the Li-B bonds, could be clearly detected owing to the thermodynamically favored interaction between LiNBH and Li metal.[18] Moreover, the N 1s and B 1s signals observed do not match those of pristine LiNBH (Figure S29, Supporting Information), further confirming that these characteristic peaks originate from reaction products formed between LiNBH and Li metal during cycling, rather than from residual LiNBH. The intensity of the peaks of Li_3N and LiB alloys decreases gradually as the depth of etching increases and the peak of Li 1s gradually shifted to low binding energy, which was closer to the position of Li^0 (Figure 4a), indicating the thickness of the layer composed of Li_3N and LiB alloys is ≈400 nm. Li_3N is well known as a typical Li ion conductor[26] and LiB alloys act as superlithiophilic sites,[27] both of which effectively contribute to alleviating the formation of Li dendrites. Cross-section SEM images of Li|$LiBH_4$-70LiNBH|Li and Li|$LiBH_4$|Li demonstrate intimate contact between Li metal electrode and solid-state electrolytes at the initial state (Figure 4d,e). After Li stripping and plating at 0.2 mA cm^{-2} for 150 cycles, noticeable defects or protrusions appear at the interface between Li and $LiBH_4$ (Figure 4g), indicating nonuniform lithium deposition, which eventually leads to dendrite formation. By comparison, when using $LiBH_4$-70LiNBH as the electrolyte, the uniform interface between Li metal and $LiBH_4$-70LiNBH is improved owing to the in situ reaction between LiNBH and Li metal (Figure 4f). This result is also verified by atomic force microscopy (AFM) measurements. After 20 cycles, when $LiBH_4$ is used as the electrolyte, the interface between Li metal and $LiBH_4$ exhibits noticeable surface roughness, with multiple protrusions appearing on the surface of Li metal, indicating the formation of Li dendrites (Figure 4h). In contrast, when using $LiBH_4$-70LiNBH as the electrolyte, the Li metal surface remains smooth, and no similar protrusions are observed (Figure 4i). Even after 30 cycles, this difference persists (Figure S30, Supporting Information). Similar phenomenon could also in situ be verified by optical microscope, which verifies that the interface between Li metal and $LiBH_4$-70LiNBH are still smooth (Figure S31, Supporting Information) after 10 cycles at a current density of 0.2 mA cm^{-2}. These results directly demonstrate the superior capability of $LiBH_4$-70LiNBH electrolyte in suppressing the formation of Li dendrites, which could be attributed to the homogeneous formation of Li_3N and LiB alloys on the surface of Li metal that is capable of guiding homogenous Li plating at the Li/$LiBH_4$-70LiNBH interface. More importantly, owing to the homogenous formation of Li_3N and LiB alloys, a high average Young's modulus of 27.96 GPa is observed for Li metal after cycling in Li|$LiBH_4$-70LiNBH|Li, 2.7 times higher than that of Li|$LiBH_4$|Li. It is reported that the surface layer with a Young's modulus larger than 3 GPa is capable of inhibiting the growth of Li dendrites.[28] Therefore, the in situ formation of ultrathin layer composed of Li_3N and LiB alloys would not only guide the homogenous Li plating, but also block the growth of Li dendrites, which synergistically enhances the capability of $LiBH_4$-70LiNBH in alleviating the growth of Li dendrites.

To evaluate the potential practical applications of $LiBH_4$-70LiNBH electrolyte, full cells coupled with commercial $Li_4Ti_5O_{12}$ cathode without any extra coating and Li metal anode are assembled and tested at the temperature of 60 °C with a current density of 0.05 C (1 C = 175 mA g^{-1}). A reversible capacity of 112 mAh g^{-1} could be obtained in the first cycle with an average discharge voltage of 1.55 V and an initial coulombic efficiency (ICE) of 80.3% (**Figure 5a**). More importantly, after 168 cycles of charge and discharge process, the $Li_4Ti_5O_{12}$ electrode delivers a high reversible capacity of 113 mAh g^{-1}, corresponding to an ultrahigh capacity retention of 98.2%, with an average coulombic efficiency of almost 100% (Figure 5b), while only a capacity of 78 mAh g^{-1} could be achieved for the cell using $LiBH_4$ as the electrolyte after only 21 cycles, indicating the superior compatibility of $LiBH_4$-70LiNBH electrolyte toward the cathode. In addition, upon increasing the current density to 0.1 C, the full cell delivers an initial reversible capacity of 128 mAh g^{-1} and a specific capacity of 135 mAh g^{-1} could still be achieved after 10 cycles (Figure S32a, Supporting Information). Impressively, upon decreasing the test temperature to 50 °C, the cell using $LiBH_4$-70LiNBH electrolyte also demonstrates a stable electrochemical property, delivering a reversible capacity of 108 mAh g^{-1} after 7 cycles at 0.05 C (Figure S32b, Supporting

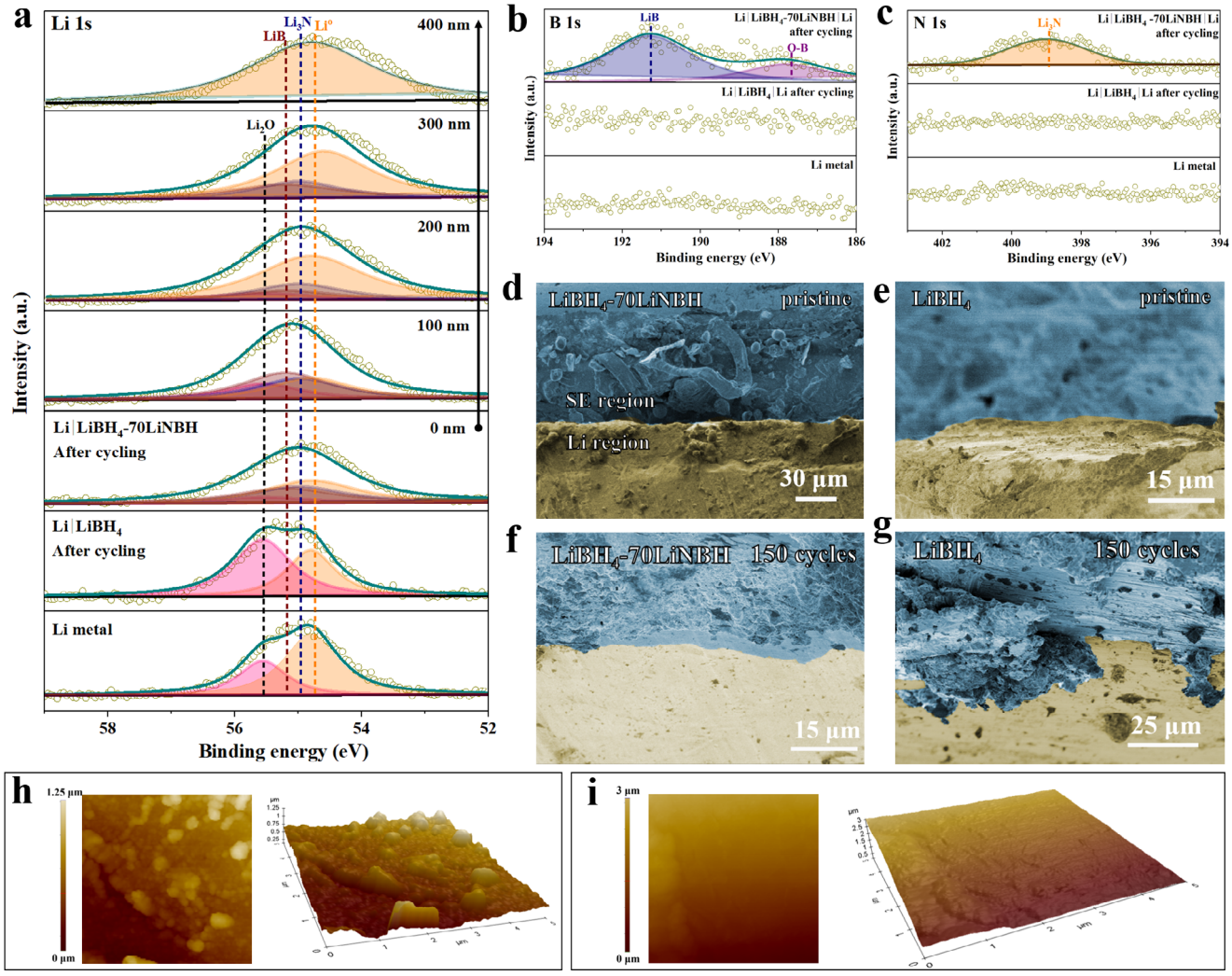

Figure 4. a) In-depth Li 1s XPS profile of and b) B 1s and c) N1s XPS profile of Li metal surface in Li|$LiBH_4$-70LiNBH|Li symmetric cells after 20 cycles at 0.2 mA cm^{-2}, with that of Li|$LiBH_4$|Li symmetric cells and Li metal included for comparison. Cross-sectional SEM images of the interfaces between Li metal and electrolytes in d,f) Li|$LiBH_4$-70LiNBH|Li and f,g) Li|$LiBH_4$|Li cell before and after cycling. The surface topography of Li metal in h) Li|$LiBH_4$|Li and i) Li|$LiBH_4$-70LiNBH|Li symmetric cells after cycling by AFM. The cycling tests were all conducted at 60 °C.

Information). Even at 30 °C, which is close to ambient conditions, the cell maintained a reversible capacity of 89 mAh g^{-1} after 3 cycles at 0.05 C (Figure S32c, Supporting Information). These results demonstrate the great potential of $LiBH_4$-70LiNBH electrolyte for practical application in ASSLMBs. In addition, the morphology of $LiBH_4$-70LiNBH pellet remains almost unchanged after exposure to air for 1 h, while the pristine $LiBH_4$ become transparent mostly due to water adsorption from air (Figure S33, Supporting Information). This indicates the resistance of $LiBH_4$-70LiNBH to the ambient atmosphere, enabling possible processing outside of glove box to some extent.

The high oxidation stability of $LiBH_4$-70LiNBH electrolyte over 5 V supports the application of current commercial 4 V-class cathode materials such as $LiCoO_2$ in ASSLBs. Thus, the as-synthesized $LiBH_4$-70LiNBH electrolyte is further investigated in ASSLBs using Li as the anode and $LiCoO_2$ as the cathode. Li_3InCl_6 with a mass ratio of 2 wt.% coated on the surface of $LiCoO_2$ using a wet-chemistry method[29] is adopted to prevent the inevitable rations between $LiBH_4$ and $LiCoO_2$. The $LiCoO_2$/$LiBH_4$-70LiNBH/Li cell shows an initial charge capacity of 128.3 mAh g^{-1} and a discharge capacity of 125.2 mAh g^{-1} (Figure 5c), corresponding to an initial Coulombic efficiency of 97.6% with typical redox reaction plateaus at 0.2 C (1 C = 120 mA h g^{-1}). The full cell exhibits an outstanding rate performance, delivering an average reversible capacity of 85.2 mAh g^{-1} upon increasing the current density to 1 C (Figure 5d). More importantly, when the current density was decreased to 0.1 C, the $LiCoO_2$/$LiBH_4$-70LiNBH/Li cell could still retain a reversible capacity of 132.2 mAh g^{-1}, corresponding to a capacity retention of 99.8%, which demonstrates the stable tolerance of $LiBH_4$-70LiNBH electrolyte for fast Li ion diffusion. A high specific capacity of 118.5 mAh g^{-1} could still be obtained at 0.2 C after 50 cycles (Figure 5e), which verifies the stable interface compatibility between the electrolyte and the electrode. Under a high current density of 0.5 C, this full cell is capable of operating for 400 cycles,

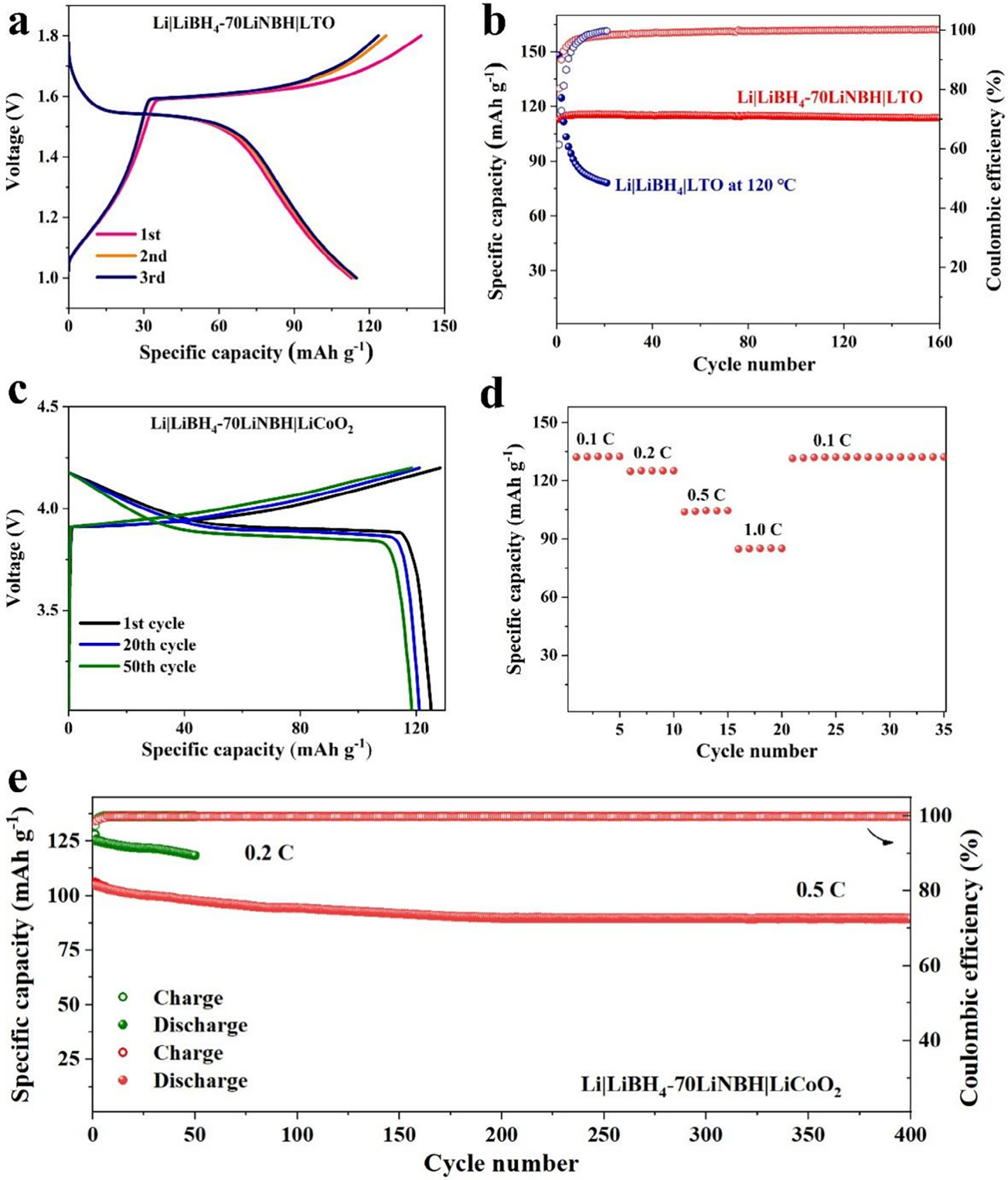

Figure 5. a) The galvanostatic discharge-charge curves and b) cycling performance of Li|$LiBH_4$-70LiNBH|LTO cell at 0.05 C, with Li|$LiBH_4$|LTO cell included for comparison. c) The galvanostatic discharge-charge curves, d) rate performance and e) cycling performance of Li|$LiBH_4$-70LiNBH|$LiCoO_2$ cell. All measurements were conducted at 60 °C, except for the Li|$LiBH_4$|LTO cell tested at 120 °C.

delivering a reversible capacity of 89.5 mAh g^{-1} with a capacity retention of 85.4%.

Moreover, the electrochemical impedance spectra of this full cell after various cycles are conducted to investigate the internal resistance change during cycling charge and discharge process. As shown in Figure S34, Supporting Information, each Nyquist plot is composed of two semicircles at high frequency and a straight line at low frequency. The intercept in the high-frequency is related to the electrolyte resistance (R_s). The first smaller semicircle is related to the Li anode/SE interfacial impedance R_{ct1}. The second larger semicircle is related to cathode/SE interfacial impedance R_{ct2} and the sloping line at low frequency is related to diffusion impedance. According to the equivalent circuit shown in Figure S35, Supporting Information, the calculated value of R_s, R_{ct1}, and R_{ct2} is shown in Table S2, Supporting Information. It is noticed that the value of cathode/SE interfacial impedance and anode is well preserved without obvious increase. This result demonstrates the stable interface compatibility between the electrolyte and the electrode, including Li metal anode and $LiCoO_2$ cathode, which also corresponds well with the stable reversible capacity of the $LiCoO_2$/$LiBH_4$-70LiNBH/Li full cell.

In addition, the electrochemical performance of $LiCoO_2$/$LiBH_4$-70LiNBH/Li full cell charging to 4.5 V was tested. As shown in Figure S36, Supporting Information, although this full cell operates well at the initial state upon charging to 4.5 V, an obvious decrease of specific capacity is observed, delivering a capacity retention of 85.2% after 50 cycles, indicating the feasibility of $LiBH_4$-70LiNBH with high-voltage cathode to some extent.

3. Conclusion

In conclusion, we report in situ space-confinement of $LiBH_4$ into porous hydrogen-deficient LiNBH to simultaneously improve Li-ion conductivity and oxidative stability of $LiBH_4$ SSEs and especially suppress the formation of Li dendrites inside of $LiBH_4$ SSEs. Induced by the strong attraction of negatively charged $H^{\delta-}$ atoms of $[BH_4]^-$ anions by Li^+ of LiNBH owing to the loss of hydrogen during the decomposition of $LiNH_2BH_3$, the deformation of $[BH_4]^-$ anions in $LiBH_4$ and the weakening of the Coulombic interaction between Li^+ and $[BH_4]^-$ anions is realized, which leads to the decrease of the Li-ion diffusion barriers observed at the interface between porous LiNBH and $LiBH_4$ down to 0.069 eV that is 1.7 times lower than $LiBH_4$. In addition, the local electron localization of $LiBH_4$ is achieved by the electron-withdrawing effect of LiNBH, which effectively blocks its electronic exchanges and hence results in the decrease of electronic conductivity of $LiBH_4$ and the increase of oxidative stability of $LiBH_4$. As a result, coupled with homogeneous interfaces between $LiBH_4$ and porous LiNBH enabled by in situ space-confinement strategy, the Li ion conductivity of $LiBH_4$ reaches 2.2×10^{-4} S cm^{-1} at 30 °C that is nearly 4 orders of magnitude higher than that of $LiBH_4$, delivering a stable voltage window of 5 V. Moreover, owing to the interaction between Li metal and LiNBH, an ultrathin layer with a high average Young's modulus of 27.96 GPa composed of Li_3N with high Li-ion conductivity and LiB alloys with high lithiophilic property is in situ formed, which could not only guide the homogenous Li plating, but also block the growth of Li dendrites. This synergistically enhances the capability of $LiBH_4$-70LiNBH in alleviating the growth of Li dendrites, leading to a critical current density (CCD) value of 7.5 mA cm^{-2} and a stable cycling life of 100 h at a high current density of 4 mA cm^{-2} with an overpotential of only 125 mV. Impressively, the ASSLMBs of $LiCoO_2$/$LiBH_4$-70LiNBH/Li cell deliver a high capacity of 89.5 mA h g^{-1} at 0.5 C after 400 cycles with a capacity retention of 85.4%. Our work provides a promising strategy to develop stable solid-state electrolyte toward building dendrite-free ASSLMBs with high energy density.

Supporting Information

Supporting Information is available from the Wiley Online Library or from the author.

Acknowledgements

This work was financially supported by the National Key R&D Program of China (no. 2023YFB2504000 to X. Yu), the National Natural Science Foundation of China (no. U2130208 and 22279020 to G. Xia), the Science and Technology Commission of Shanghai Municipality (no. 23ZR1406500 to G. Xia).

Conflict of Interest

The authors declare no conflict of interest.

Data Availability Statement

The data that support the findings of this study are available in the supplementary material of this article.;

Keywords

all-solid-state Li metal batteries, electron localization, lithium borohydride, solid-state electrolyte

Received: April 27, 2025
Revised: July 8, 2025
Published online:

[1] a) Z. Shadike, H. Lee, O. Borodin, X. Cao, X. Fan, X. Wang, R. Lin, S.-M. Bak, S. Ghose, K. Xu, C. Wang, J. Liu, J. Xiao, X.-Q. Yang, E. Hu, *Nat. Nanotechnol.* **2021**, *16*, 549; b) S. Tu, B. Zhang, Y. Zhang, Z. Chen, X. Wang, R. Zhan, Y. Ou, W. Wang, X. Liu, X. Duan, L. Wang, Y. Sun, *Nat. Energy* **2023**, *8*, 1365.

[2] a) X. Wang, G. Pawar, Y. Li, X. Ren, M. Zhang, B. Lu, A. Banerjee, P. Liu, E. J. Dufek, J.-G. Zhang, J. Xiao, J. Liu, Y. S. Meng, B. Liaw, *Nat. Mater.* **2020**, *19*, 1339; b) Y. Fang, S. L. Zhang, Z.-P. Wu, D. Luan, X. W. Lou, *Sci. Adv.* **2021**, *7*, abg3626; c) H. Zhang, S. Ju, G. Xia, X. Yu, *Sci. Adv.* **2022**, *8*, abl8245.

[3] a) G. Wang, C. Chen, Y. Chen, X. Kang, C. Yang, F. Wang, Y. Liu, X. Xiong, *Angew. Chem., Int. Ed.* **2020**, *59*, 2055; b) G. Xu, J. Li, C. Wang, X. Du, D. Lu, B. Xie, X. Wang, C. Lu, H. Liu, S. Dong, G. Cui, L. Chen, *Angew. Chem., Int. Ed.* **2021**, *60*, 7770; c) B. Han, Z. Zhang, Y. Zou, K. Xu, G. Xu, H. Wang, H. Meng, Y. Deng, J. Li, M. Gu, *Adv. Mater.* **2021**, *33*, 2100404.

[4] a) Y.-G. Lee, S. Fujiki, C. Jung, N. Suzuki, N. Yashiro, R. Omoda, D.-S. Ko, T. Shiratsuchi, T. Sugimoto, S. Ryu, J. H. Ku, T. Watanabe, Y. Park, Y. Aihara, D. Im, I. T. Han, *Nat. Energy* **2020**, *5*, 299; b) B. Zahiri, A. Patra, C. Kiggins, A. X. B. Yong, E. Ertekin, J. B. Cook, P. V. Braun, *Nat. Mater.* **2021**, *20*, 1392; c) E. A. Wu, S. Banerjee, H. Tang, P. M. Richardson, J.-M. Doux, J. Qi, Z. Zhu, A. Grenier, Y. Li, E. Zhao, G. Deysher, E. Sebti, H. Nguyen, R. Stephens, G. Verbist, K. W. Chapman, R. J. Clément, A. Banerjee, Y. S. Meng, S. P. Ong, *Nat. Commun.* **2021**, *12*, 1256; d) P. Shi, J. Ma, M. Liu, S. Guo, Y. Huang, S. Wang, L. Zhang, L. Chen, K. Yang, X. Liu, Y. Li, X. An, D. Zhang, X. Cheng, Q. Li, W. Lv, G. Zhong, Y.-B. He, F. Kang, *Nat. Nanotechnol.* **2023**, *18*, 602.

[5] Y.-K. Sun, *ACS Energy Lett.* **2020**, *5*, 3221.

[6] L. Zhou, C. Y. Kwok, A. Shyamsunder, Q. Zhang, X. Wu, L. F. Nazar, *Energy Environ. Sci.* **2020**, *13*, 2056.

[7] L. Ye, X. Li, *Nature* **2021**, *593*, 218.

[8] M. B. Dixit, B. S. Vishugopi, W. Zaman, P. Kenesei, J.-S. Park, J. Almer, P. P. Mukherjee, K. B. Hatzell, *Nat. Mater.* **2022**, *21*, 1298.

[9] W. Xia, Y. Zhao, F. Zhao, K. Adair, R. Zhao, S. Li, R. Zou, Y. Zhao, X. Sun, *Chem. Rev.* **2022**, *122*, 3763.

[10] M. Matsuo, S.-i. Orimo, *Adv. Energy Mater.* **2011**, *1*, 161.

[11] a) A. Unemoto, M. Matsuo, S.-i. Orimo, *Adv. Funct. Mater.* **2014**, *24*, 2267; b) W. D. Richards, L. J. Miara, Y. Wang, J. C. Kim, G. Ceder, *Chem. Mater.* **2016**, *28*, 266; c) S. Payandeh, R. Asakura, P. Avramidou, D. Rentsch, Z. Łodziana, R. Černý, A. Remhof, C. Battaglia, *Chem. Mater.* **2020**, *32*, 1101.

[12] a) R. Zettl, K. Hogrefe, B. Gadermaier, I. Hanzu, P. Ngene, P. E. de Jongh, H. M. R. Wilkening, *J. Phys. Chem. C* **2021**, *125*, 15052; b) V. Gulino, L. Barberis, P. Ngene, M. Baricco, P. E. de Jongh, *ACS Appl. Energy Mater.* **2020**, *3*, 4941.

[13] a) J. Lefevr, L. Cervini, J. M. Griffin, D. Blanchard, *J. Phys. Chem. C* **2018**, *122*, 15264; b) Y. S. Choi, Y.-S. Lee, K. H. Oh, Y. W. Cho, *Phys. Chem. Chem. Phys.* **2016**, *18*, 22540.

[14] Z. Lu, F. Ciucci, *Chem. Mater.* **2017**, *29*, 9308.

[15] a) Y. Wei, Y. Yang, Z. Chen, P. Gao, Q. Ma, M. Gao, C. Yan, Z. Wu, Y. Jiang, J. Chen, X. Yu, Z. Li, X. Zhang, Y. Liu, M. Gao, W. Sun, H. Pan, *Adv. Mater.* **2023**, *35*, 2304285; b) L. Hu, H. Wang, Y. Liu, F. Fang, B. Yuan, R. Hu, *ACS Appl. Mater. Interfaces* **2022**, *14*, 1260.

[16] F. Mo, J. Ruan, S. Sun, Z. Lian, S. Yang, X. Yue, Y. Song, Y.-N. Zhou, F. Fang, G. Sun, S. Peng, D. Sun, *Adv. Energy Mater.* **2019**, *9*, 1902123.

[17] H. Su, J. Li, Y. Zhong, Y. Liu, X. Gao, J. Kuang, M. Wang, C. Lin, X. Wang, J. Tu, *Nat. Commun.* **2024**, *15*, 4202.

[18] Z. Wang, Y. Wang, Z. Zhang, X. Chen, W. Lie, Y.-B. He, Z. Zhou, G. Xia, Z. Guo, *Adv. Funct. Mater.* **2020**, *30*, 2002414.

[19] A. T. Luedtke, T. Autrey, *Inorg. Chem.* **2010**, *49*, 3905.

[20] K. Shimoda, K. Doi, T. Nakagawa, Y. Zhang, H. Miyaoka, T. Ichikawa, M. Tansho, T. Shimizu, A. K. Burrell, Y. Kojima, *J. Phys. Chem. C* **2012**, *116*, 5957.

[21] R. S. Apu, N. Hasan, R. I. Haque, A. Kabir, M. H. Rashid, *AIP Adv.* **2025**, *15*, 035043.

[22] a) X. Kang, Z. Fang, L. Kong, H. Cheng, X. Yao, G. Lu, P. Wang, *Adv. Mater.* **2008**, *20*, 2756; b) K. Shimoda, K. Doi, T. Nakagawa, Y. Zhang, Y. Kojima, *J. Phys. Chem. C* **2016**, *116*, 5957.

[23] X. He, Y. Zhu, Y. Mo, *Nat. Commun.* **2017**, *8*, 15893.

[24] M. A. Ratner, *Phys. Today* **1997**, *50*, 66.

[25] a) F. Lu, Y. Pang, M. Zhu, F. Han, J. Yang, F. Fang, D. Sun, S. Zheng, C. Wang, *Adv. Funct. Mater.* **2019**, *29*, 1809219; b) D. Blanchard, A. Nale, D. Sveinbjörnsson, T. M. Eggenhuisen, M. H. W. Verkuijlen, T. V. Suwarno, A. P. M. Kentgens, P. E. de Jongh, *Adv. Funct. Mater.* **2015**, *25*, 184.

[26] a) M. S. Kim, Z. Zhang, J. Wang, S. T. Oyakhire, S. C. Kim, Z. Yu, Y. Chen, D. T. Boyle, Y. Ye, Z. Huang, W. Zhang, R. Xu, P. Sayavong, S. F. Bent, J. Qin, Z. Bao, Y. Cui, *ACS Nano* **2023**, *17*, 3168; b) X. Ji, S. Hou, P. Wang, X. He, N. Piao, J. Chen, X. Fan, C. Wang, *Adv. Mater.* **2020**, *32*, 2002741.

[27] C. Wu, H. Huang, W. Lu, Z. Wei, X. Ni, F. Sun, P. Qing, Z. Liu, J. Ma, W. Wei, L. Chen, C. Yan, L. Mai, *Adv. Sci.* **2020**, *7*, 1902643.

[28] X. Shen, R. Zhang, X. Chen, X.-B. Cheng, X. Li, Q. Zhang, *Adv. Energy Mater.* **2020**, *10*, 1903645.

[29] C. Wang, J. Liang, M. Jiang, X. Li, S. Mukherjee, K. Adair, M. Zheng, Y. Zhao, F. Zhao, S. Zhang, R. Li, H. Huang, S. Zhao, L. Zhang, S. Lu, C. V. Singh, X. Sun, *Nano Energy* **2020**, *76*, 105015.